applied sciences

MDPI

Article

Opportunities for Producing Laser Beam Spot-Welded Joints in Nimonic 80A Superalloys

Călin Lucian Burcă [1], Olimpiu Karancsi [2], Dragoş Vâlsan [1], Ion Mitelea [1], Corneliu Marius Crăciunescu [1] and Ion-Dragoș Uțu [1,*]

[1] Department of Materials and Fabrication Engineering, Politehnica University Timisoara, Bulevardul Mihai Viteazul nr. 1, 300222 Timisoara, Romania; lucian.burca@student.upt.ro (C.L.B.); dragos.valsan@student.upt.ro (D.V.); ion.mitelea@upt.ro (I.M.); corneliu.craciunescu@upt.ro (C.M.C.)

[2] Department of Oral Implantology and Prosthetic Restorations on Implants, Victor Babes University of Medicine and Pharmacy Timisoara, Eftimie Murgu Sq., 300041 Timisoara, Romania; karancsi.olimpiu@umft.ro

* Correspondence: dragos.utu@upt.ro

Abstract

The present work aims to investigate the microstructure and mechanical properties of laser beam spot welds in the superalloy Nimonic 80 A. Considering the importance of this innovative process in the manufacturing of engineering components for high-security industries, it is necessary to study the influence of the welding thermal cycle on the microstructure and mechanical properties of welded joints. The rapid heating/cooling, melting, and re-solidification phenomena that occur during welding modify the metallurgical characteristics of the weld compared with the microstructure of the base metal. Because the energy density is high and the process duration is very short, the microstructure obtained after solidification is fine dendritic in the central area of the joint and columnar in the weld–base metal transition zone. For the same reasons, the heat-affected zone (HAZ) is slightly extended. The increase in the size of the crystalline grains in the HAZ is negligible due to the low diffusivity of the nickel-based γ solid solution matrix, which inhibits the rapid migration of grain boundaries during the welding process. Metallographic analyses were performed using optical microscopy and scanning electron microscopy. The microhardness values, 152–168 HV0.05 in the weld and 180–190 HV0.05 in the base metal, together with the tensile–shear strength values (760–780 N/mm^2) obtained at room temperature, demonstrate that the proposed welding process is appropriate and feasible for engineering applications involving Nimonic 80A superalloys.

Keywords: Nimonic 80 A; laser spot welding; microstructure properties

Academic Editors: Jure Krolo, Branimir Lela and Zoran Jurković

Received: 26 February 2026
Revised: 19 March 2026
Accepted: 20 March 2026
Published: 21 March 2026

1. Introduction

Nickel-based superalloys contain alloying elements, such as Cr, Mo, Fe, W, Co, Al, and Ti, in their chemical composition. They are particularly widespread and can be found in commercial products such as Inconel, Hastelloy, Monel, and Nimonic, used in demanding applications. In general, Ni and its alloy semi-finished products have variable thicknesses, ranging from foils to plates of several tens of millimeters and variable dimensions, from microminiature electronic components to tank cars [1–5].

Their structure and chemical composition ensure high mechanical strength and high corrosion stability even at 90% of nickel's melting temperature. The phenomenon is explained by the maintenance of the same crystalline lattice (c.f.c) from ambient temperature to melting temperature.

Among these, the superalloy Nimonic 80 A, which can be hardened through artificial aging heat treatment, is used in applications such as the following [1]:

- Engineering of gas turbines;
- Engine exhaust valves;
- Die-casting inserts and cores;
- Nuclear boiler tube parts.

The material exhibits outstanding performance in service conditions, characterized by strong resistance to elevated temperatures, creep, and corrosion/oxidation. These properties result from both the alloying elements in its chemical composition and the strengthening mechanisms involved, such as solid solution strengthening, strain hardening, and precipitation hardening achieved through artificial aging [2,4,5]. The metallurgical and technological weldability of Ni-based superalloys is not covered in detail in the specialized literature; instead, specifications on nickel welding can be found. Nimonic 80 A, however, has specific elements, and its use in extremely precise and critical fields requires a deep understanding of the structural transformations that occur during the melting welding process, in order to judiciously select the technological regime parameters. At present, nickel and nickel-based alloys are joined using the most common processes, such as welding, brazing, and soldering. The main welding processes used for joining these materials include gas tungsten arc welding (GTAW), shielded metal arc welding (SMAW), resistance spot welding (RSW), explosive welding, electron beam welding, laser welding, and plasma welding [6–18]. The main objective of the present study is to understand the effect of the thermal cycle during laser spot welding on the microstructure and mechanical properties of the nickel-based superalloy Nimonic 80A, which is essential for ensuring the reliability and operational safety of welded components.

In the laser spot welding process, high energy is used to join two pieces. The coherent laser light beam is focused on the area to be welded and transfers enough energy to melt and join the metal surfaces together. The main advantages offered by this innovative process are as follows [19–29]:

- Accurate control of penetration, preventing deformation or indentation on the rear surface of the lower component;
- A very narrow beam diameter (under 1 mm), which produces a minimal heat-affected zone;
- A significantly shorter processing time, roughly three to four times faster than resistance spot welding;
- High process stability and repeatability, resulting in consistent weld quality and less need for rework.

In recent decades, some research works have emerged investigating the effects of certain welding technological parameters on the mechanical behavior of welded joints made from Ni-based alloys [11,13,14].

Thus, M. Bemani and M. Pouranvari [21] analyzed the microstructure and mechanical properties of spot-welded joints by resistance in the superalloy Nimonic 263. They demonstrated that following the solidification of the molten core, a dendritic structure with secondary carbides is obtained, and the heat-affected zone underwent a constitutional liquation of carbides (Ti, Mo) in the base material. Their findings also demonstrated that the mechanical properties of the welded joint depend primarily on the dimensions of the fusion zone and the depth of the electrode indentation. Yaxing

https://doi.org/10.3390/app16063054

Tong, Guoliang Zhu, and Sanbao Lin [9] studied the gas tungsten arc welding (GTAW) process of the ZGH4142 superalloy, precipitation-hardened and manufactured by laser powder bed fusion (LPBF). Microstructural analysis, together with finite element modeling, was applied to elucidate the influence of linear energy and welding direction on the microstructure and mechanical behavior of the welded joint. The results showed that increasing the linear energy reduced the cooling rate, increased the geometry of the molten zone, and the fine equiaxed grains in the center of the weld became coarser.

T. Vilaro et al. [22] studied the microstructure of the Nimonic 263 superalloy produced using the selective laser melting (SLM) process. Due to the extremely short interaction time between the laser beam and the powder particles—typically only a few milliseconds—the resulting microstructures are in a non-equilibrium state. Consequently, post-processing heat treatments are required either to homogenize the microstructure and promote precipitation hardening or to relieve residual stresses.

Guangyi Ma et al. [23] highlighted the characteristics of the electron beam welding process of the Ni-based alloy 686. SEM, EDS, and XRD analyses highlighted the presence of secondary phases at the grain boundaries in the fusion zone, which affect the mechanical properties and corrosion resistance.

Although several studies have examined the resistance spot welding (RSW) of nickel-based superalloys [20–26], there is currently no published research that thoroughly investigates the microstructural evolution during welding or the mechanical properties of joints produced by laser beam spot welding. Given the growing industrial relevance of laser welding in the fabrication of Ni-based superalloy components, it is important to assess the feasibility of applying this advanced process to products manufactured in large volumes.

2. Materials and Experimental Procedure

This study focused on the spot welding of Nimonic 80 A superalloy sheets using a laser beam. The sheets had a thickness of 1.6 mm and were subjected to a solution annealing treatment at 1150 °C for 2 min prior to welding, followed by air cooling. The nickel oxide layer that formed on the surface during heat treatment was removed by polishing with a fine abrasive stone to prevent any influence on the welding process.

The chemical composition of the superalloy (Table 1) was determined by optical emission spectrometry using a Thermo ARL QuantoDesk spectrometer (Burladingen, Germany). Mechanical characterization at room temperature included static tensile testing, performed on a Zwick/Roell testing machine with a load capacity of 250 kN (Ulm, Germany), and hardness measurements carried out using an HVS-10A1 Vickers hardness tester (Beijing, China). The mean values of mechanical characteristics at room temperature are presented in Table 2.

Table 1. Chemical composition of the Nimonic 80 superalloy.

Element	wt%
Ni	Balance
Cr	20.11
Ti	2.65
Al	1.2
Si	0.49
Mn	0.63
Fe	0.92
C	0.06
S	0.01

Table 2. Mechanical properties at room temperature of the Nimonic 80 superalloy.

Mechanical strength, Rm	876 N/mm^2
Yield strength, Rp 0.2	618 N/mm^2
Elongation at braking, A5	37%
Necking, Z	51%
Hardness, HV	186 daN/mm^2

The welding process was realized by Razotek welding equipment from Dezhou, China (Figure 1), which has the following as its main components:

- LASER weld in the device;
- Cooling equipment (chiller);
- Welding gun;
- A wire feeder unit (for welding with filler metal);
- Gas tank: argon or nitrogen.

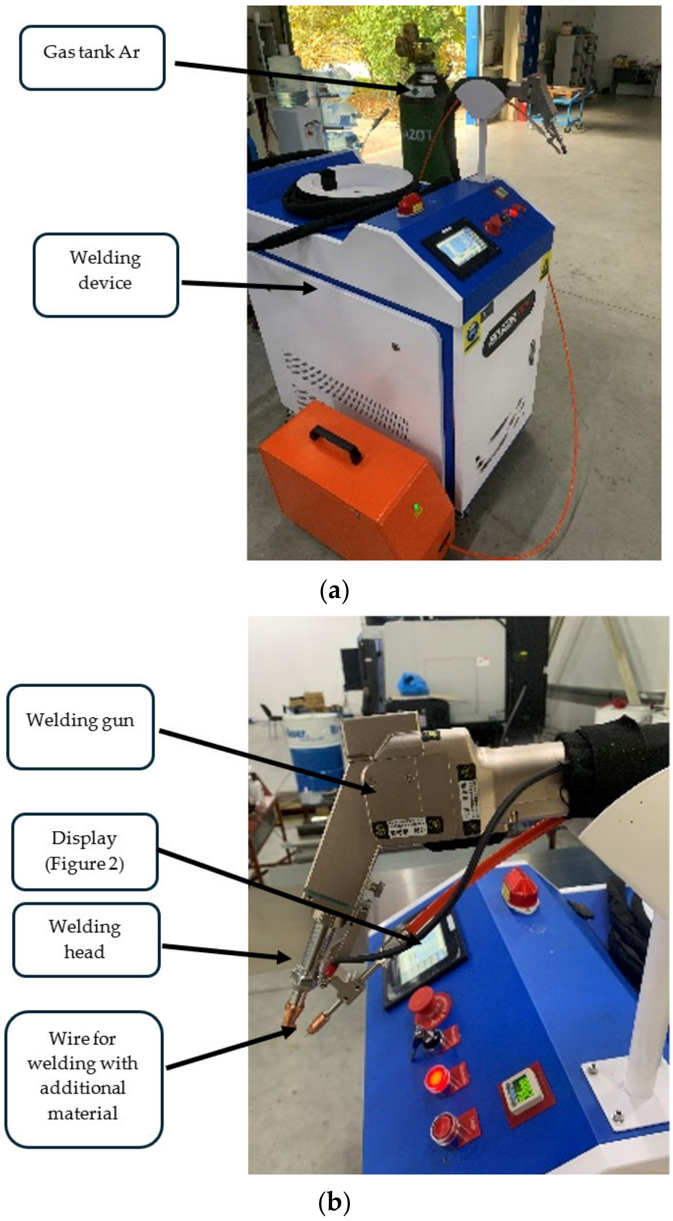

Figure 1. LASER Raycus welding device (RFL C1500, Dezhou, China): (**a**) overview; (**b**) welding gun.

The laser can operate in two modes, the CW (continuous welding) or the PWM (power wave modulation) function, and intermittent or pulsed through the argon arc (pulsed TIG) or QCW (quasi-continuous wave) function. Figure 2 shows the main welding parameters that can be modified in this second mode of operation:

- Laser power (W);
- Diameter (amplitude) of the spot: 0–5 mm;
- Frequency of the spot: 1–200 Hz;
- Wire speed (cm/min);
- Type of oscillation: 8 types of oscillation;
- Pre-gas time and post-gas (s);
- Laser type: fiber laser;
- Laser wavelength: 1070 nm.

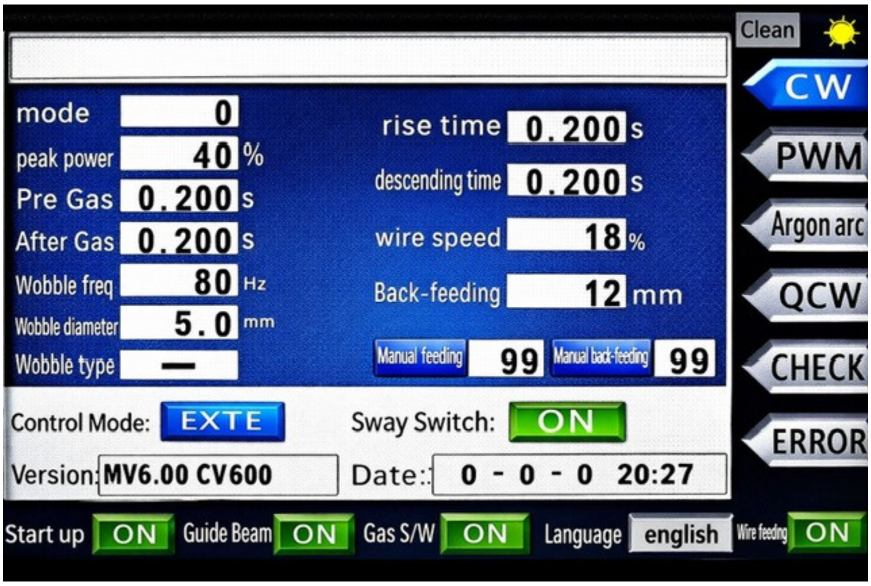

Figure 2. Touch screen panel of the welding device.

The fiber laser offers advantages such as excellent beam quality, high electrical and optical efficiency, increased reliability, low maintenance, high stability, maneuverability, and ease of use.

The welding conditions used in the experiments were as follows:

- Base metal: Nimonic 80 A;
- Plate thickness: 1.6 mm;
- Type of welded joint: spot overlap;
- Shielding gas: nitrogen, $p > 99.99\%$;
- Mode of operation: intermittent or pulsed (argon arc);
- Working method: manual welding with coordinated guidance of the welding head (Figure 3).

To investigate the mechanical properties of welded joints, a tensile–shear test was performed at room temperature. The modes of fracture of the welds were determined through macro- and micro-fractographic analyses.

To examine the microstructure in the various regions of the joint, the welded specimens were prepared following standard metallographic procedures. The weld microstructure was revealed using a chemical etchant composed of 15 mL of HCl, 10 mL of acetic acid, and 5 mL of HNO_3. Microstructural observations were carried out using both optical microscopy and scanning electron microscopy (SEM). Semi-quantitative chemical composition analysis was conducted with a TESCAN electron microscope equipped with an energy-dispersive X-ray spectroscopy (EDX) system, operating at an accelerating voltage of 15 kV. The Vickers microhardness of the different weld zones was determined using a Buehler Vickers microhardness tester with an applied load of 50 g.

Figure 3. Positioning of the laser welding head.

3. Evaluation and Interpretation of Experimental Results

3.1. Macroscopic Analysis of Welded Joints

Table 3 presents the technological parameters for laser spot welding using the intermittent argon arc operating mode, without filler material, at a peak laser power of 1450 W. The beam oscillation frequency was 50 Hz with an oscillation amplitude of 5 mm, and the laser beam had a circular oscillation shape. The 2 s post-gas time allowed for a reduction in oxidation on the surface of the welded points.

Table 3. Welding regime parameters.

Laser power	1450 W
Pre-gas time	0.7 s
Post-gas time	2.0 s
Spot oscillation frequency	50 Hz
Diameter of the spot oscillation	5.0 mm
Shape/type of the oscillation	circular
Impulse	5%
Time between impulses	1 level

A number of welded spots arranged successively or in parallel were made. The appearance of the welded spots is shown in Figure 4.

Characteristic of these welded joints is the formation of a crater in the middle of the point, whose dimensions depend on the power of the laser, which defines the volume of the molten metal and the solidification conditions. For optimal welding conditions, the surface of the point should be silver, possibly slightly purple- or yellow-colored depending on the moment of contact between the surface and the air. If the post-gas time is too short or if the welding head is lifted too quickly from the surface of the components when the process is interrupted, a slight oxidation of the surface will be observed.

https://doi.org/10.3390/app16063054

Under these conditions, a total of 3 samples were made with 2 parallel welded points each, and 3 samples with a single welded point each, for the tensile–shear test.

The appearance of the samples with the welded points is shown in Figure 5, both on the outer surface and on the opposite side.

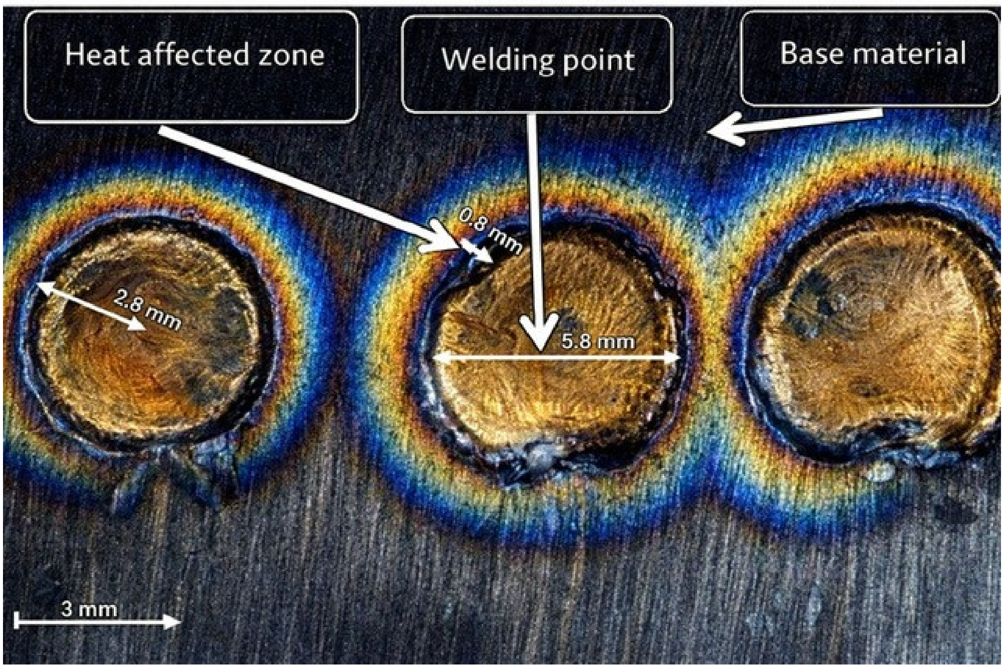

(a)

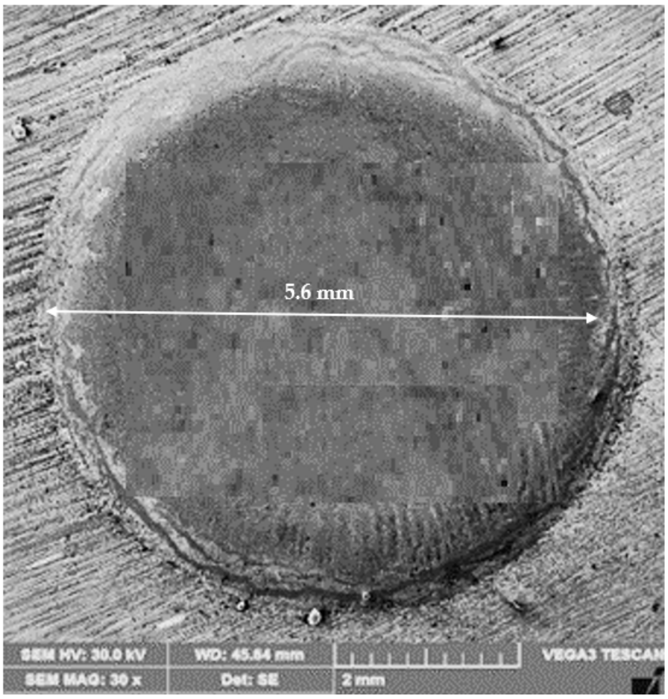

(b)

Figure 4. *Cont.*

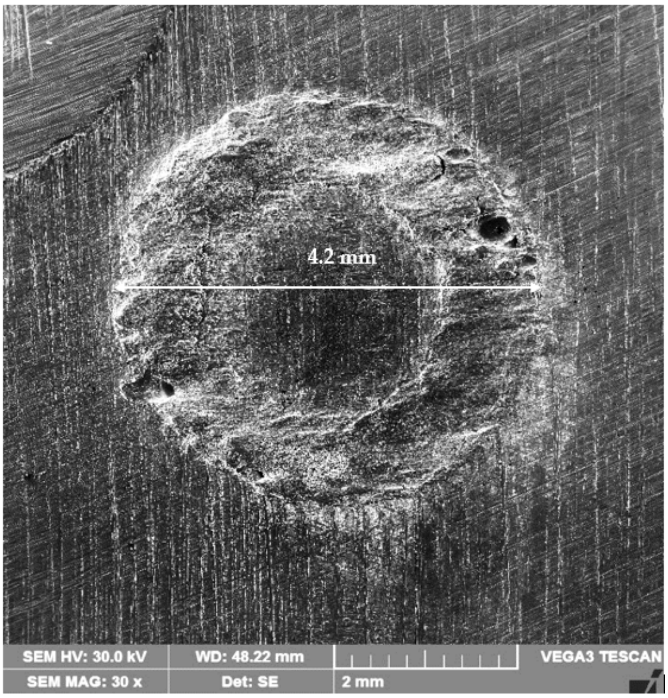

(c)

Figure 4. View of Nimonic 80 A welding points: (**a**) optical microscopic view, exterior surface; (**b**) SEM image, exterior surface; (**c**) SEM image, opposite side of the external surface.

3.2. Tensile–Shear Tests

To evaluate the mechanical performance of the welds, tensile–shear tests were carried out at room temperature on specimens joined by a single laser spot weld. The sample dimensions were as follows: length L = 400 mm, width b = 18 mm, and thickness s = 1.6 mm. The experiments were performed on a calibrated Zwick/Roell tensile testing machine with a maximum load capacity of 250 kN. All tests were conducted at a temperature of +20 °C.

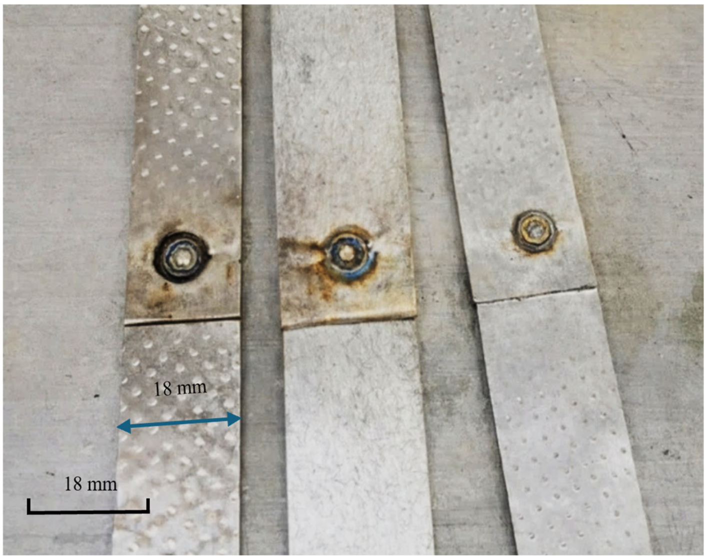

(**a**)

Figure 5. *Cont.*

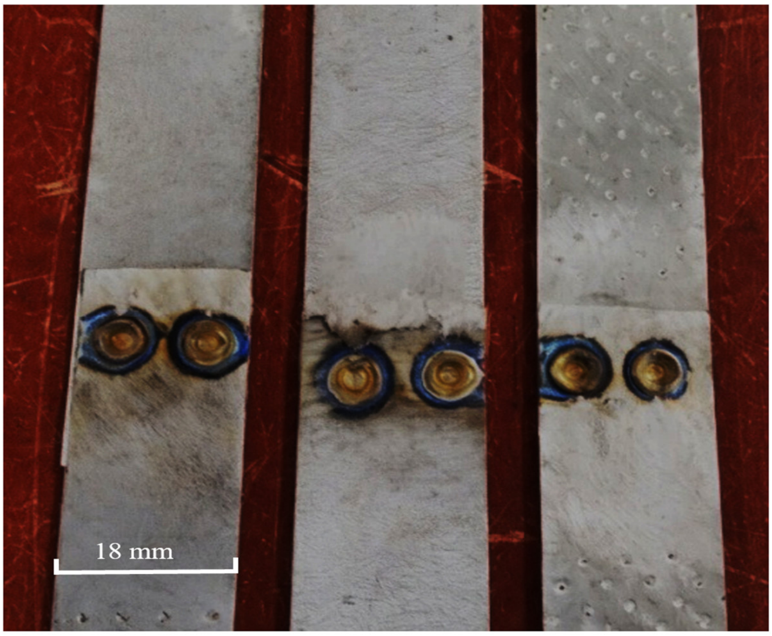

(**b**)

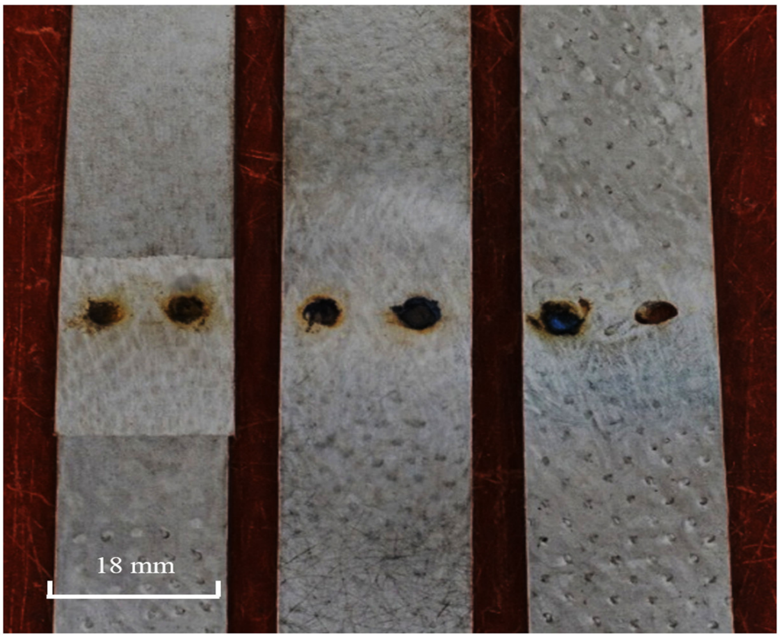

(**c**)

Figure 5. Appearance of the samples of the base material Nimonic 80 A: (**a**) 1 welding point; (**b**) 2 welding points on the exterior surface; (**c**) 2 welding points on the opposite of the exterior surface.

The welded specimens were secured using the hydraulic grips of the testing machine, positioned at a distance of 110 mm, which represented the reference gauge length for deformation measurement. The loading rate was set to 0.1 mm/min. The applied force was measured using the machine's load cell, which had a measurement uncertainty of 0.1%, while deformation was determined from the displacement of the machine's crosshead. The obtained results are presented in Table 4 and illustrated by the curves in Figure 6, indicating that the mechanical strength of the weld is comparable to that of the base material.

Table 4. Tensile–shear tests' results.

Sample	Maximum Force F_{max}, N	Maximum Elongation A, mm	Shear Stress σ_f, N/mm^2
1	3520	0.246	764
2	4000	0.27	789
3	3260	0.26	757

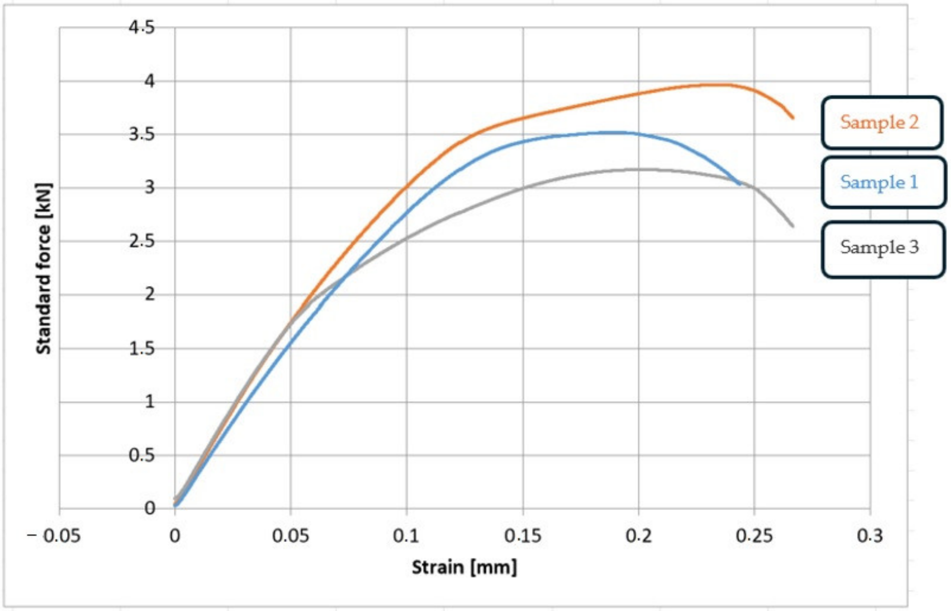

Figure 6. Static traction curves for specimens with two welded points.

3.3. Fractographic Investigations

Macro-fractographic observations (Figure 7a) together with micro-fractographic analyses (Figure 7b,c) of the breaking surfaces indicate that the fracture mechanism is predominantly ductile and is preceded by considerable plastic deformation. The presence of numerous cavities on the fracture surface is characteristic of ductile failure, while the concave morphology results from the nucleation, growth, and coalescence of voids during plastic deformation. Under shear loading, the fracture plane is not perpendicular to the loading axis; consequently, the cavities exhibit an elongated, parabolic morphology oriented along the direction of the principal stress (Figure 7c). In addition to variations in cavity size (Figure 7b), other fracture features such as cleavage facets and intergranular fracture are also observed, in some regions being even more pronounced than the void structures.

3.4. Structural Analyses and Microhardness Measurements

The macroscopic examination of a cross-section through the welded joint was performed to highlight any possible metal continuity defects. Figure 8a shows a macrograph of the welded joint, indicating that there is no evidence of cracks, undercuts, or lack of penetration in the fusion zone of the welded joint. The columnar grain structure observed in the fusion zone of the welded joint (Figure 8a) reflects the direction of the highest heat flow and rapid heat dissipation during the welding process. Furthermore, the absence of visible defects in the weld indicates that the selected experimental welding parameters were appropriate and close to optimal.

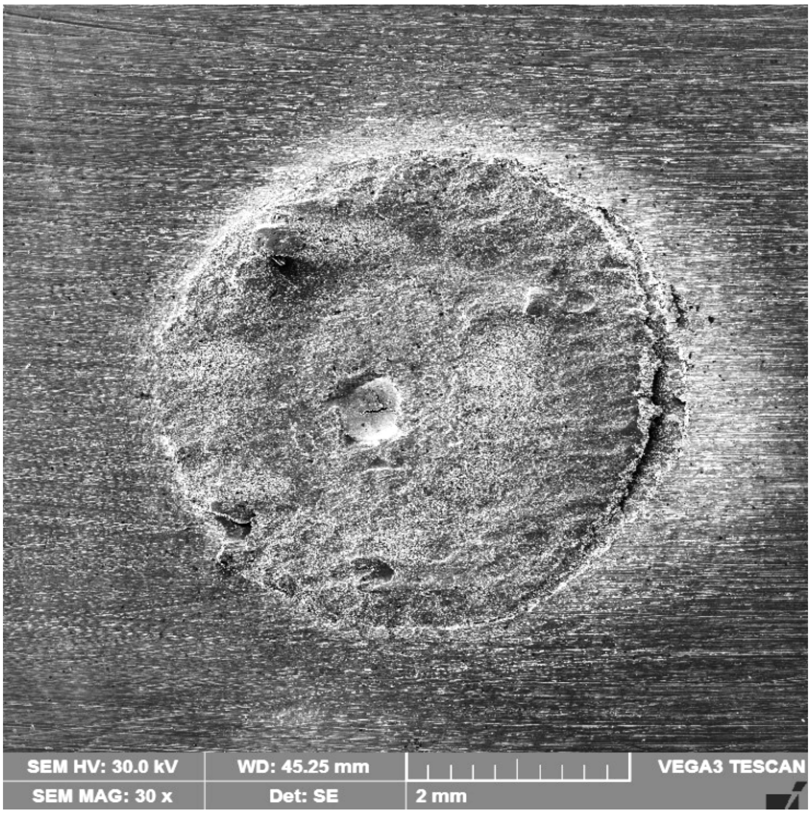

(**a**)

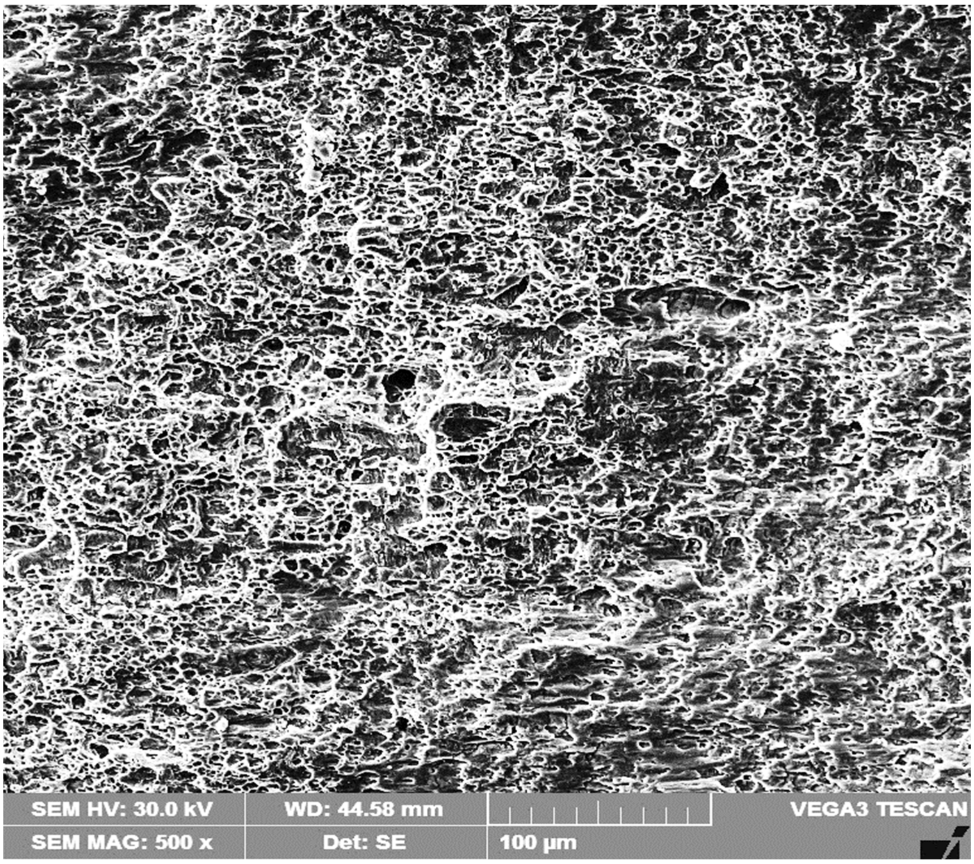

(**b**)

Figure 7. *Cont.*

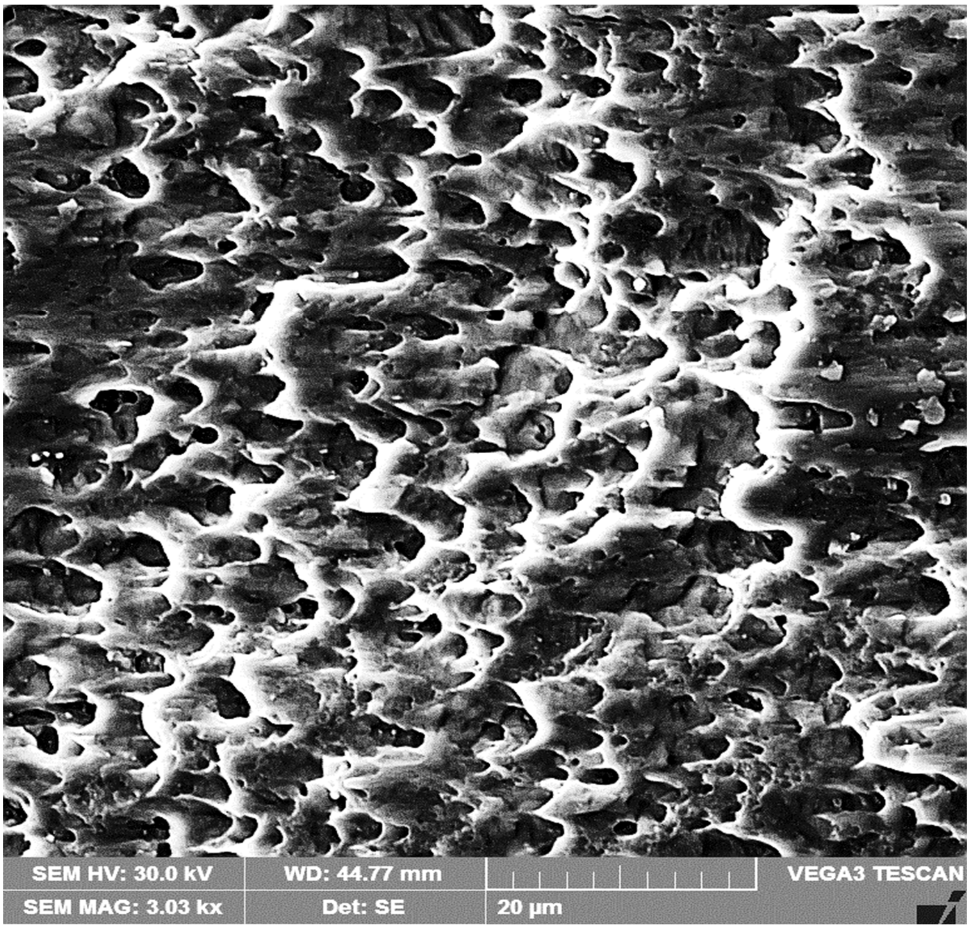

(**c**)

Figure 7. SEM image of the tearing surface of the welding point: (**a**) ×30; (**b**) ×500; (**c**) ×3000.

Microhardness measurements (Figure 8b) reveal that in the weld zone, there are somewhat lower values (152–168 HV 0.05), compared to the base metal (180–190 HV 0.05). The somewhat lower microhardness values in the weld can be explained by the limitation of precipitation phenomena of intermetallic phases with a brittle character, a phenomenon caused by the high cooling rate from the peak temperature reached during welding. The very short duration of the fusion process delays the separation of these phases.

The investigation of the effect that the welding thermal cycle has on the transformations occurring in the welded joints was carried out by optical and electron microscopy examinations. As shown in Figure 9, three distinct microstructural regions can be distinguished in the welded joint: the fusion zone, where melting and subsequent solidification occur during the welding process; the heat-affected zone (HAZ), where solid-state transformations are induced by the thermal cycle; and the base material, which remains unaffected by the welding heat input.

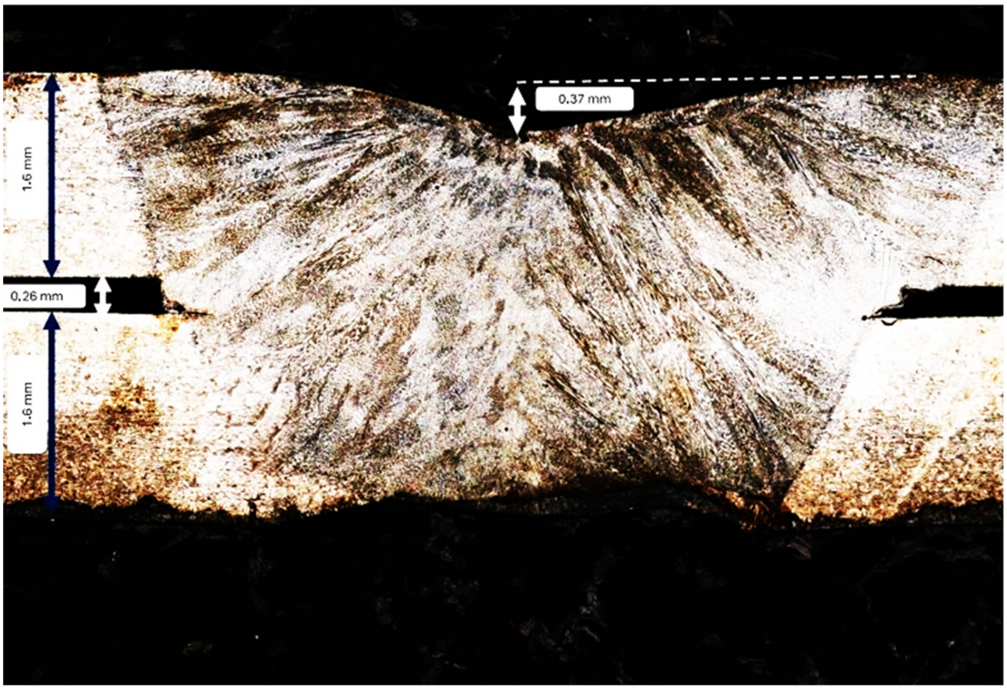

(a)

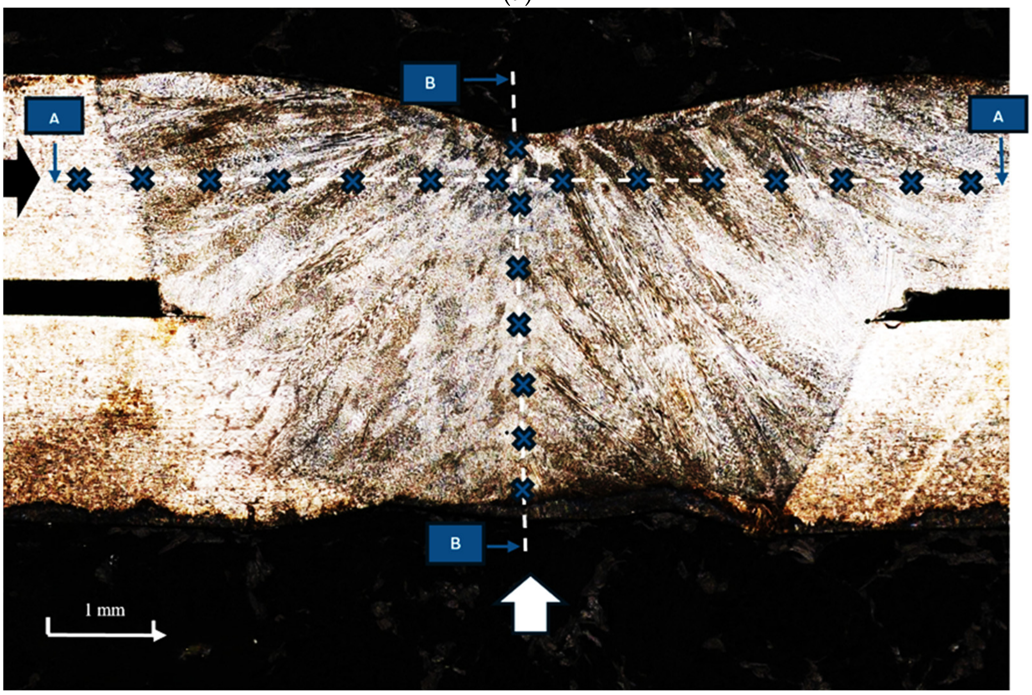

Section A-A

HV0.05

1	2	3	4	5	6	7	8	9	10	11	12	13	14
184	168	162	160	158	157	154	157	161	161	166	167	168	168

Section B-B

HV0.05

1	2	3	4	5	6	7
163	160	155	152	154	154	153

(b)

Figure 8. Macrographic image (**a**) and microhardness values (**b**) of the welded joint.

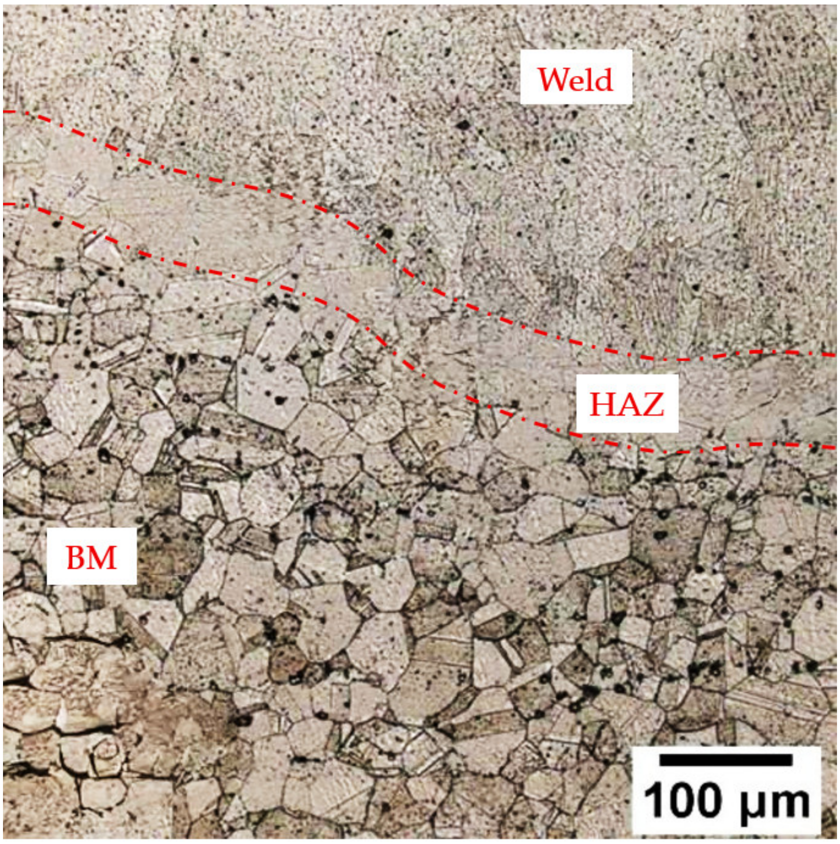

(a)

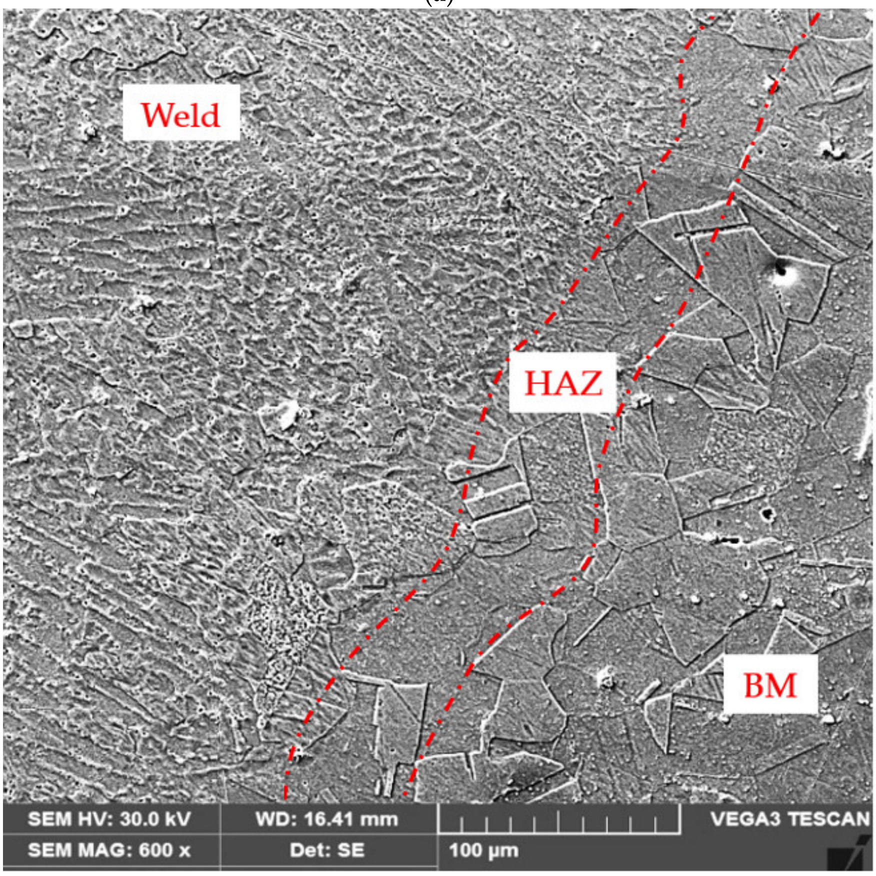

(b)

Figure 9. Microstructural zones of the welded joint: (**a**) optical microscopy image; (**b**) SEM image.

The microstructure of the base metal heat-treated with the solution (Figure 10a) consists of equiaxed grains of γ solid solution with clear boundaries between them. This heat treatment ensured the almost complete dissolution of alloying elements in the austenitic matrix. In several grains, annealing twins can be observed, and at the boundaries of some of them, a small proportion of intermetallic phases appears. The extent of the heat-affected zone (HAZ) is limited due to the very short welding duration and the high power density of the heat source. In the HAZ, the average grain size increased slightly from 6 to 11 μm (Figure 9). This limited grain growth can be attributed to the low diffusivity of the nickel-based matrix, which has a face-centered cubic crystal structure, thereby restricting rapid grain boundary migration during the welding process [24]. Moreover, the rapid heating associated with welding prevented the complete dissolution of the intermetallic phases initially present in the base metal microstructure. The fine-grained structure of the central weld zone (Figure 10c) is the result of the rapid solidification process, respectively, due to a high degree of undercooling of the molten metal pool. The higher the degree of undercooling, the smaller the size of the crystallization nuclei, the greater their number, and, consequently, the finer the resulting structure. The section adjacent to the central fusion zone exhibits a fine dendritic microstructure (Figure 10b). The variation in microstructural architecture from fine dendrites to columnar dendrites is explained by changes in the thermal gradient. Thermal gradients in a weld pool are steeper in regions close to the fusion line than inside the weld. These steep thermal gradients, predominant near the fusion line, favor columnar dendritic growth.

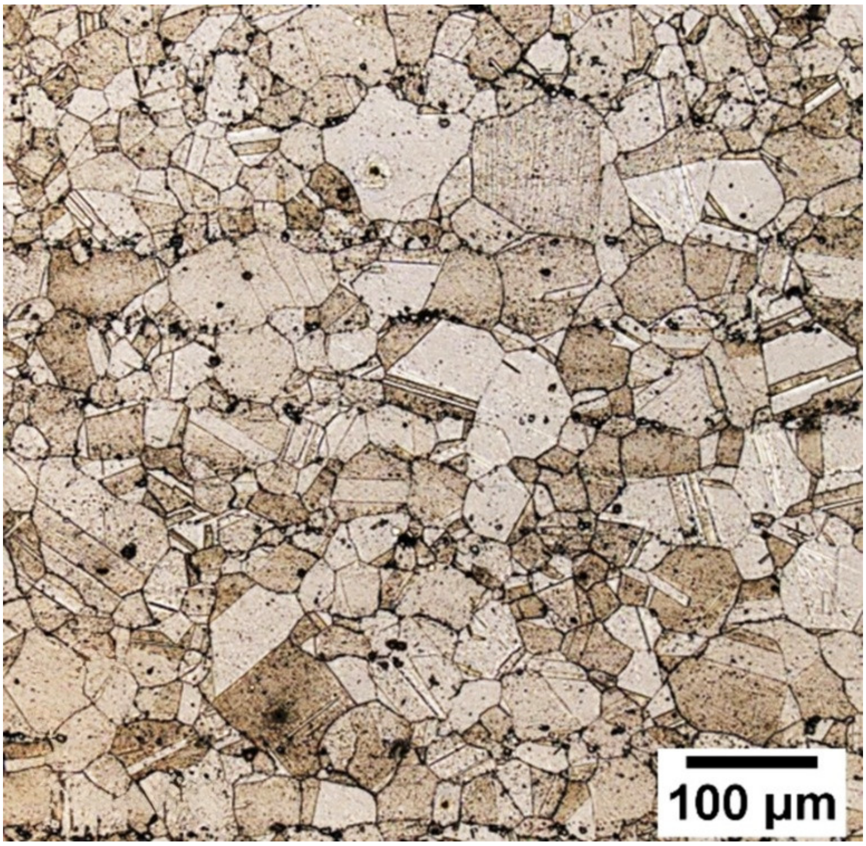

(**a**)

Figure 10. *Cont.*

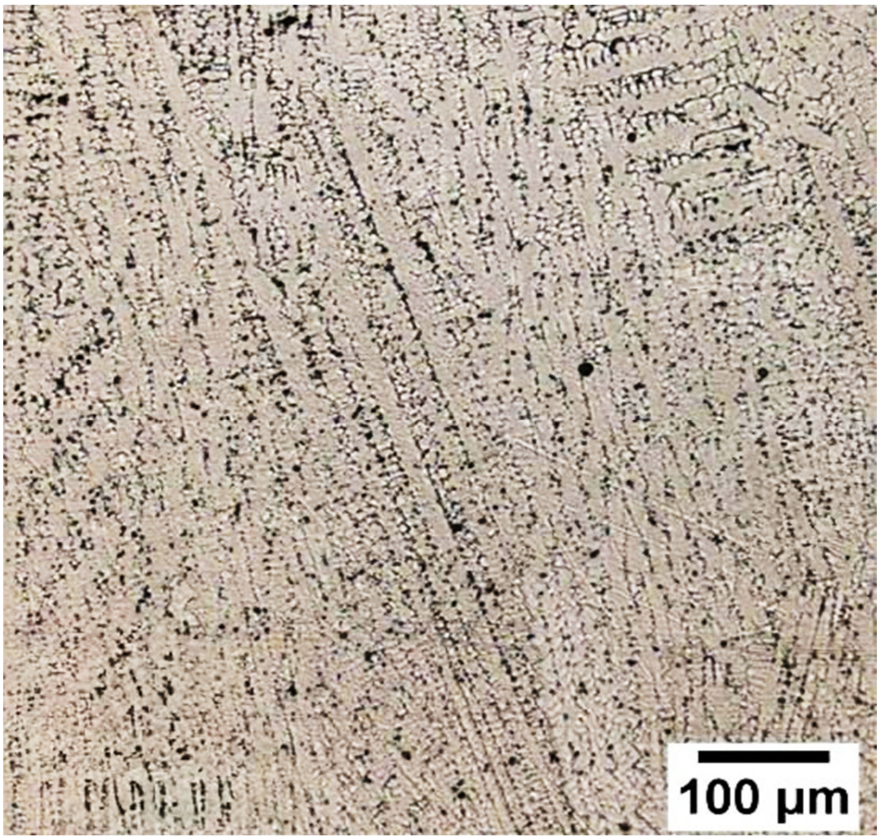

(b)

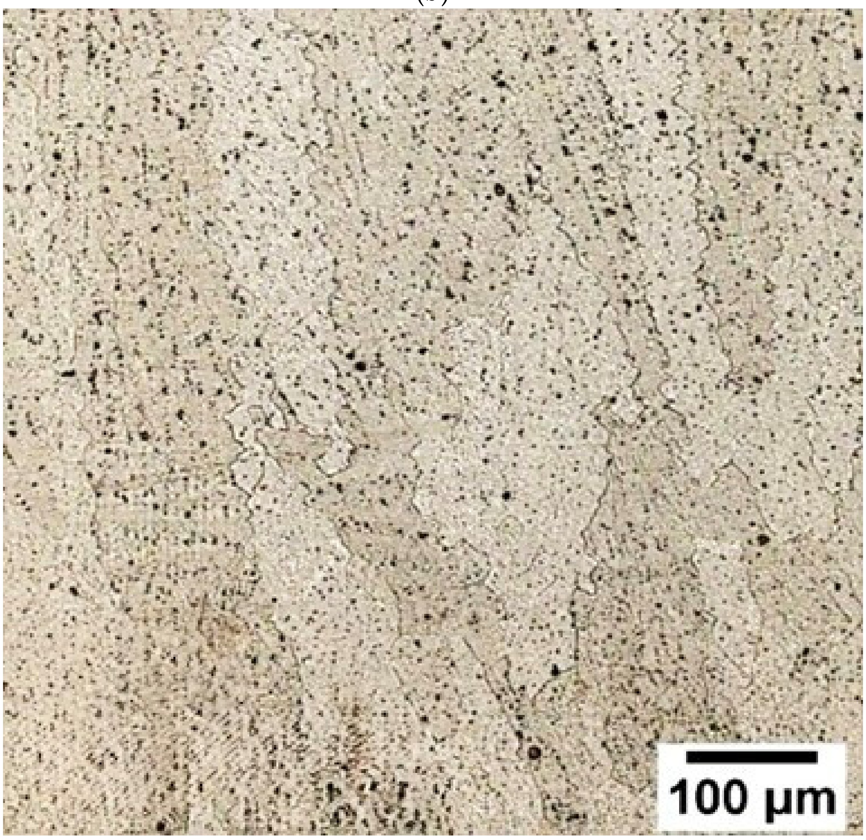

(c)

Figure 10. Microstructure of welded joint areas: (**a**) base metal; (**b**) weld marginal zone; (**c**) weld central zone.

3.5. EDX Analysis

Energy-dispersive X-ray analyses carried out on a portion of the outer surface (Figures 11 and 12) of the welded point highlight changes in chemical composition caused by the thermal and dynamic action of the heat source. They manifest through the following:

- Evaporation of alloying elements;
- Chemical interactions between the alloy constituents;
- Reactions between the molten metal and the surrounding environment;
- Constitutional liquation and dendritic segregation;
- Irregular gas protection.

During the solidification of the molten metal bath, the cooling rates specific to laser beam welding are so high that they cause significant segregation of alloying elements due to constitutional liquation. Since the welded alloy has a high Ni content, which has a strong segregation potential and is also an element that forms intermetallic phases, variations within wide limits of the concentrations of this element and Ti can be expected in the peripheral area of the weld point (Figure 12).

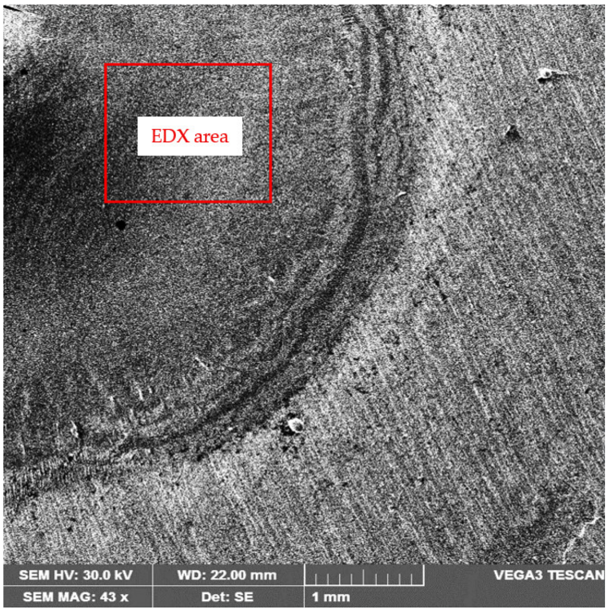

(**a**)

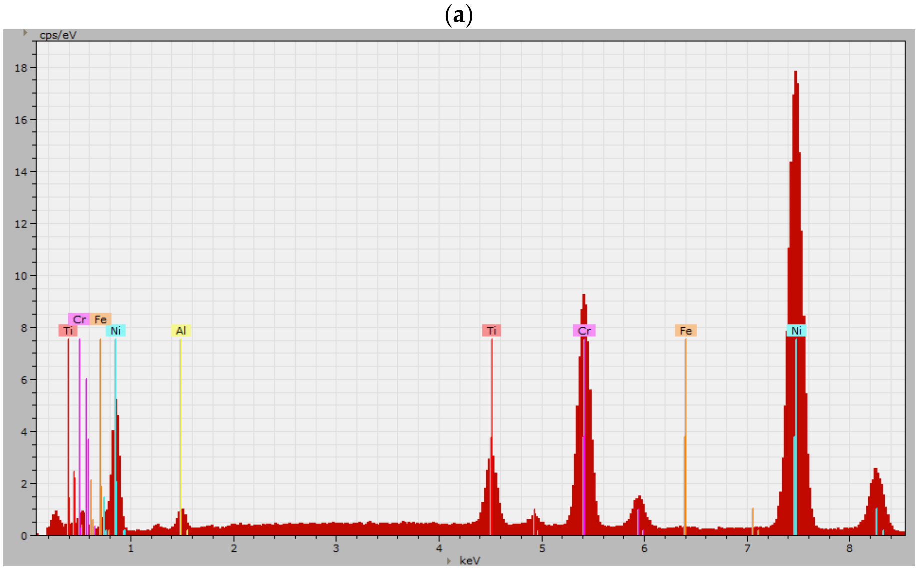

(**b**)

Figure 11. *Cont.*

Element	Series	Mass C. (wt.%)	Norm. C. (wt.%)	Atom C. (at.%)	Error (1 Sigma) (wt.%)
Ti	K series	5.12	5.75	6.53	0.18
Ni	K series	61.53	69.09	63.98	1.56
Cr	K series	19.24	21.60	22.58	0.54
Al	K series	2.95	3.32	6.68	0.20
Fe	K series	0.22	0.24	0.24	0.04
	Total	89.06	100.00	100.00	

(**c**)

Figure 11. SEM image (**a**), energy-dispersive X-ray spectrum (**b**), and chemical composition of a microregion from the upper part of the weld point (**c**).

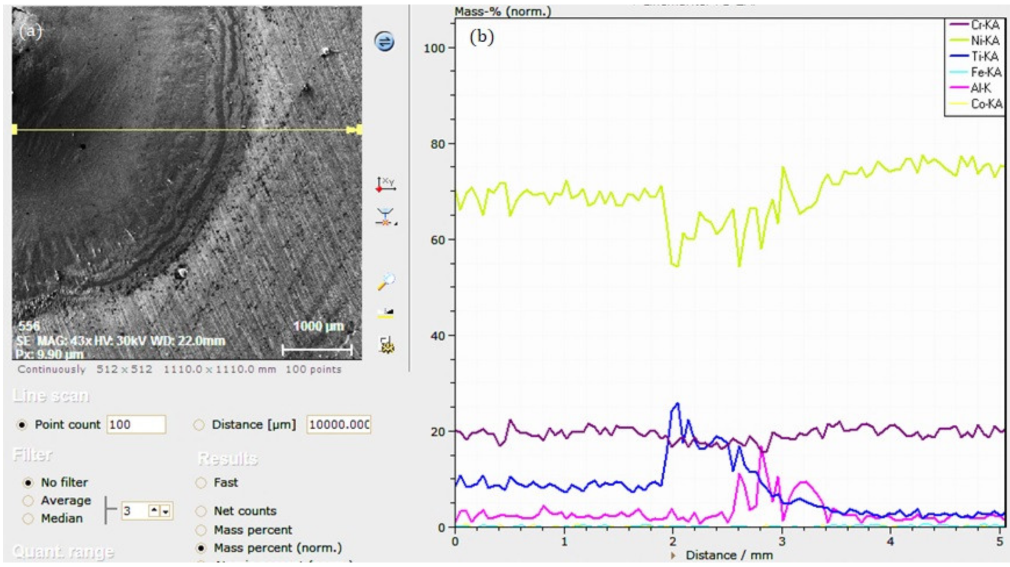

Figure 12. Microstructure (**a**) and the linear variation in the alloying element concentrations (**b**) in the region between the upper part of the welded joint and the base metal.

If limited variations in the concentrations of Cr, Ni, Al, Ti, and Fe occur in the base metal, in the outer area of the weld point, wide variations are observed in Ni (from approx. 55% by weight to approx. 70% by weight), Cr (from approx. 18% by weight to approx. 22% by weight), Ti (from approx. 10% by weight to approx. 25% by weight), and Al (from approx. 0.2% by weight to approx. 4% by weight). These variations are explained by the phenomenon of constitutional liquation that appears in the heat-affected zone (HAZ) of the welded joint [30,31]. The thermal cycles in the HAZ cause partial melting of secondary phase particles present along grain boundaries if the peak temperature reached in the HAZ lies between the eutectic temperature and the solidus point of the base metal.

By the partial melting of these particles and a part of the surrounding matrix, a heterogeneous liquid in alloying elements is formed, which infiltrates the grain boundaries.

Carrying out the same investigations in a microregion from the lower part of the welded point (Figures 13 and 14) confirms that the segregation phenomena of alloying elements due to constitutional liquation persist, but their intensity is lower. Thus, the concentration of Ni has values of 68–72% in the welded point and 70–75% in the base metal, the concentrations of Cr and Al have practically identical values (approx. 21% Cr and approx. 3% Al) in both investigated zones, and the concentration of Ti has values of 5.1–6.2% in the welded point and 1.9–2.2% in the base metal.

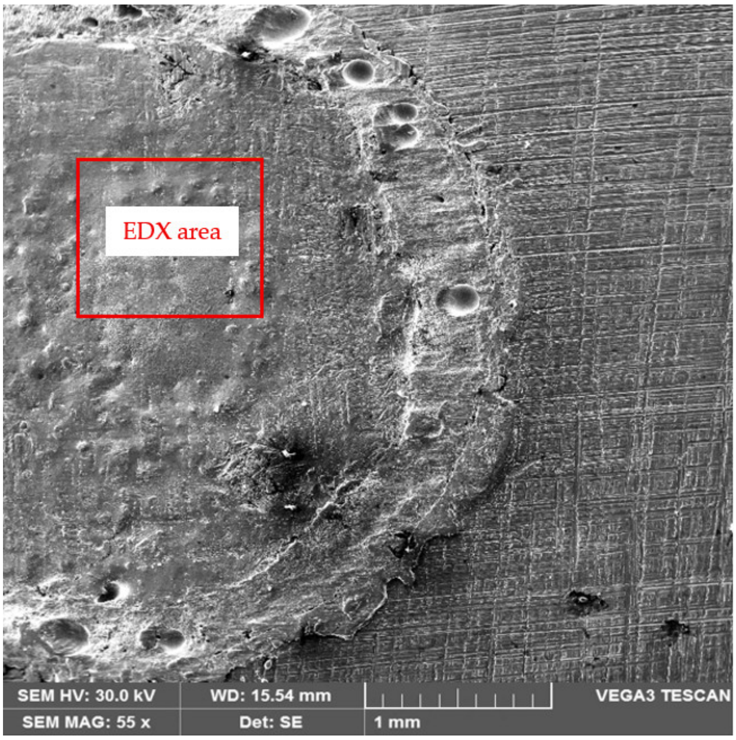

(**a**)

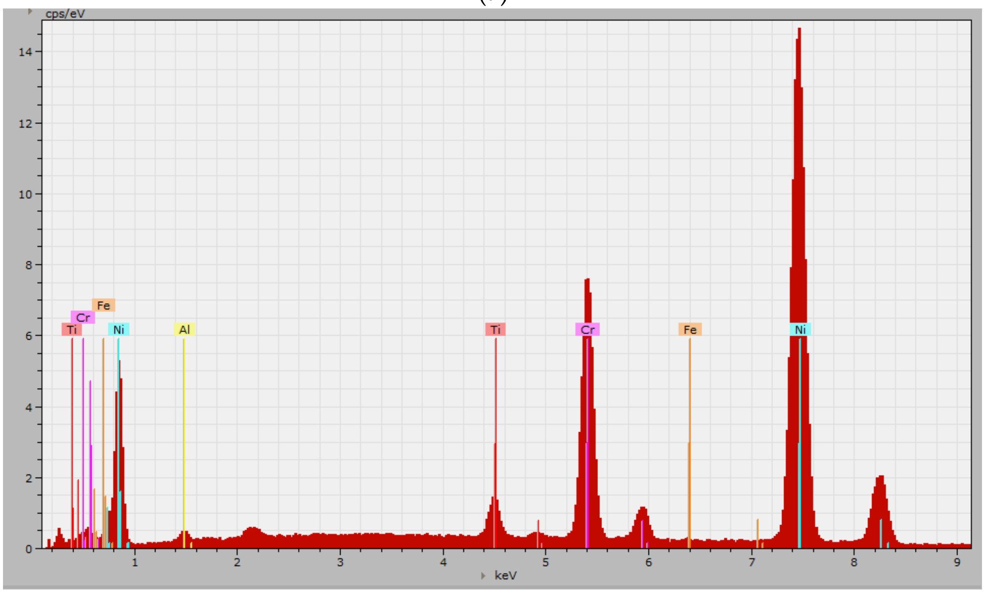

(**b**)

Element	Series	Mass C. (wt.%)	Norm. C. (wt.%)	Atom C. (at.%)	Error (1 Sigma) (wt.%)
Ti	K series	2.55	2.96	3.46	0.11
Ni	K series	64.40	74.50	71.15	1.63
Cr	K series	18.45	21.35	23.01	0.52
Al	K series	0.94	1.09	2.27	0.09
Fe	K series	0.09	0.10	0.11	0.03
	Total	86.44	100.00	100.00	

(**c**)

Figure 13. SEM image (**a**), energy-dispersive X-ray spectrum (**b**), and chemical composition of a microregion from the lower part of the welded point (**c**).

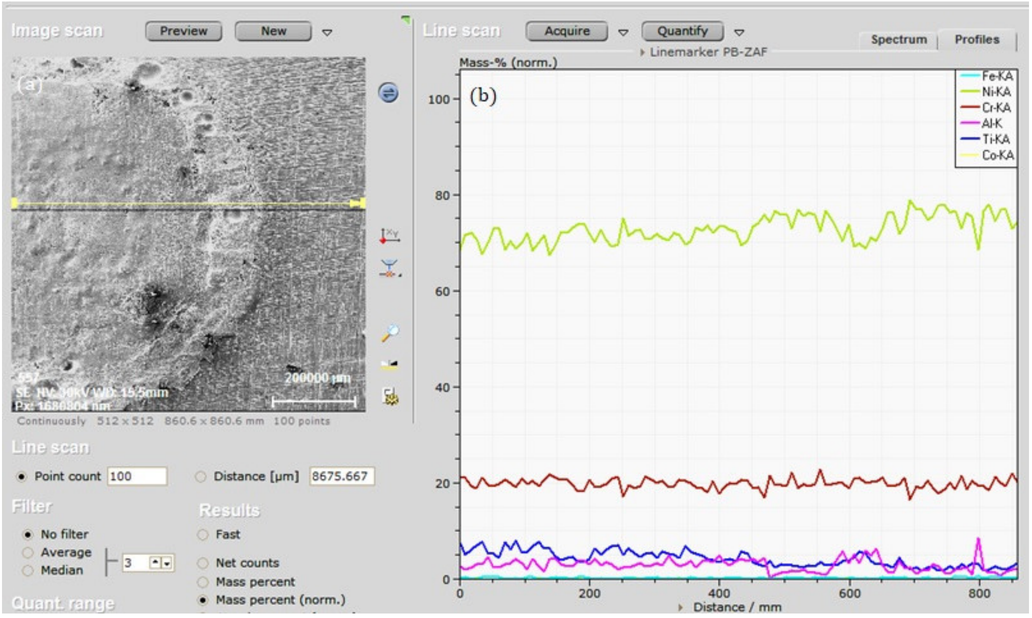

Figure 14. Microstructure (**a**) and linear variation in alloying element concentrations (**b**) in the interface region between the lower part of the welded spot and the base metal.

4. Conclusions

The results of microstructural investigations and mechanical tests performed on laser beam spot welds of the Nimonic 80 A superalloy led to the following conclusions:

a. The parameters of the laser welding process have a significant influence on the microstructural and mechanical characteristics of homogeneous welded joints.
b. The weld microstructure is fine dendritic in the marginal zone and columnar in the central zone.
c. The weld microhardness is slightly lower than that of the base metal, due to the reduction in the proportion of intermetallic phase particles and the growth of grains in this region.
d. Elongated, parabolic-shaped cavities present on the fracture surface examined by scanning electron microscopy demonstrate its ductile nature and are oriented with their axis towards the principal stress.
e. The effects of welding parameters on tensile–shear strength showed that the breaking load has high values and that the test used can provide a useful reference for the laser beam spot welding process.

Author Contributions: Conceptualization, I.M. and I.-D.U.; methodology, C.L.B., O.K., D.V., I.M., C.M.C. and I.-D.U.; investigation, C.L.B., O.K., D.V., I.M., C.M.C. and I.-D.U.; writing—original draft preparation, I.M. and I.-D.U.; writing—review and editing, C.L.B., I.M. and I.-D.U.; visualization, C.L.B., O.K., D.V., I.M., C.M.C. and I.-D.U.; supervision, I.M. and I.-D.U. All authors have read and agreed to the published version of the manuscript.

Funding: This research received no external funding.

Institutional Review Board Statement: Not applicable.

Informed Consent Statement: Not applicable.

Data Availability Statement: The original contributions presented in this study are included in the article. Further inquiries can be directed to the corresponding author.

Conflicts of Interest: The authors declare no conflicts of interest.

References

1. Pollock, T.M. Alloy design for aircraft engines. *Nat. Mater.* **2016**, *15*, 809–815. [CrossRef]
2. Roth, H.A.; Davis, C.L.; Thomson, R.C. Modeling solid solution strengthening in nickel alloys. *Metall. Mater. Trans. A* **1997**, *28*, 1329–1335. [CrossRef]
3. Chittewar, S.L.; Patil, N.G. Surface integrity of conventional and additively manufactured nickel superalloys: A review. *Mater. Today Proc.* **2021**, *44*, 701–708. [CrossRef]
4. Gudivada, G.; Pandey, A.K. Recent developments in nickel-based superalloys for gas turbine applications: Review. *J. Alloys Compd.* **2023**, *963*, 171128. [CrossRef]
5. Wei, J.; Li, Y.; Liu, C.; Ma, S.; Gu, J.; Lu, M.; Song, M. Enhanced mechanical properties of a nickel-based superalloy by regulating Laves and δ phases via hot rolling deformation. *J. Mater. Res. Technol.* **2025**, *36*, 7344–7350. [CrossRef]
6. David, S.A.; Siefert, J.A.; DuPont, J.N.; Shingledecker, J.P. Weldability and weld performance of candidate nickel-base superalloys for advanced ultra-supercritical fossil power plants—Part I: Fundamentals. *Sci. Technol. Weld. Join.* **2015**, *20*, 532–552. [CrossRef]
7. Vemanaboina, H.; Gundabattini, E.; Akella, S.; Rao, A.C.U.M.; Buddu, R.K.; Ferro, P.; Berto, F. Mechanical and Metallurgical Properties of CO_2 Laser Beam INCONEL 625 Welded Joints. *Appl. Sci.* **2021**, *11*, 7002. [CrossRef]
8. Henderson, M.B.; Arrell, D.; Heobel, M.; Marchant, G.; Larsson, R. Nickel-based superalloy welding practices for industrial gas turbine applications. *Sci. Technol. Weld. Join.* **2004**, *9*, 13–21. [CrossRef]
9. Tong, Y.; Zhu, G.; Lin, S. Microstructural evolution and strengthening mechanisms of gas tungsten arc welded nickel-based superalloy joints processed by laser powder bed fusion: Effects of welding direction and heat input. *J. Mater. Process. Technol.* **2025**, *346*, 119098. [CrossRef]
10. Lippold, J.C. *Welding Metallurgy and Weldability*; John Wiley & Sons: Hoboken, NJ, USA, 2014.
11. Zapirain, F.; Zubiria, F.; Garciandía, F.; Tolosa, I.; Chueca, S.; Goiria, A. Development of laser welding of Ni-based superalloys for aeronautic engine applications (experimental process and obtained properties). *Phys. Procedia* **2011**, *12*, 105–112. [CrossRef]
12. Kathuria, Y.P. Some aspects of laser surface cladding in the turbine industry. *Surf. Coat. Technol.* **2000**, *132*, 262–269. [CrossRef]
13. Sharma, S.K.; Biswas, K.; Nath, A.K.; Manna, I.; Dutta Majumdar, J. Microstructural change during laser welding of Inconel 718. *Optik* **2020**, *218*, 165029. [CrossRef]
14. Shehbaz, T.; Hashmi, J.A.; Khan, F.N.; Baig, M.N.; Junaid, M. Comparative analysis of microstructural evolution and mechanical performance in laser and electron beam welded Udimet 720 superalloy joints. *Mater. Today Commun.* **2025**, *49*, 114310. [CrossRef]
15. Zhang, D.; Niu, W.; Cao, X.; Liu, Z. Effect of standard heat treatment on the microstructure and mechanical properties of selective laser melting manufactured Inconel 718 superalloy. *Mater. Sci. Eng. A* **2015**, *644*, 32–40. [CrossRef]
16. Guo, W.; Dong, S.; Guo, W.; Francis, J.A.; Li, L. Microstructure and mechanical characteristics of a laser welded joint in SA508 nuclear pressure vessel steel. *Mater. Sci. Eng. A* **2015**, *625*, 65–80. [CrossRef]
17. Hou, T.; Li, Y.; Wang, D.; Wang, Y.; Vilotic, M. Experiments and modeling of microstructural and mechanical behaviors of laser-welded Ni-based superalloy at high temperatures. *Chin. J. Aeronaut.* **2025**, *38*, 103249. [CrossRef]
18. Talei, M.G.; Ghoreishi, M. Microstructure and mechanical properties of laser weld of selective laser melted IN625 superalloy. *J. Mater. Res. Technol.* **2025**, *36*, 10157–10168. [CrossRef]
19. Alizadeh-Sh, M.; Pouranvari, M.; Marashi, S.P.H. Welding metallurgy of stainless steels during resistance spot welding—Part II: Heat affected zone and mechanical performance. *Sci. Technol. Weld. Join.* **2015**, *20*, 512–521. [CrossRef]
20. Bemani, M.; Pouranvari, M. Microstructure and mechanical properties of dissimilar nickel-based superalloys resistance spot welds. *Mater. Sci. Eng. A* **2020**, *773*, 138825. [CrossRef]
21. Bemani, M.; Pouranvari, M. Resistance spot welding of Nimonic 263 nickel-based superalloy: Microstructure and mechanical properties. *Sci. Technol. Weld. Join.* **2020**, *25*, 28–36. [CrossRef]
22. Vilaro, T.; Colin, C.; Bartout, J.D.; Nazé, L.; Sennour, M. Microstructural and mechanical approaches of the selective laser melting process applied to a nickel-base superalloy. *Mater. Sci. Eng. A* **2012**, *534*, 446–451. [CrossRef]
23. Ma, G.; Wu, D.; Niu, F.; Zou, H. Microstructure evolution and mechanical property of pulsed laser welded Ni-based superalloy. *Opt. Lasers Eng.* **2015**, *72*, 39–46. [CrossRef]
24. Ashtiani, H.R.R.; Zarandooz, R. Microstructural and mechanical properties of resistance spot weld of Inconel 625 superalloy. *Int. J. Adv. Manuf. Technol.* **2016**, *84*, 607–619. [CrossRef]
25. Harkins, F.G. Spot welding nickel and nickel alloys. *Weld. J.* **1950**, *29*, 3s–12s.
26. Martín, O.; Tiedra, P.D.; San-Juan, M. Combined effect of resistance spot welding and precipitation hardening on tensile shear load bearing capacity of A286 superalloy. *Mater. Sci. Eng. A* **2017**, *688*, 309–314. [CrossRef]
27. Tiedra, P.D.; Martín, Ó.; San-Juan, M. Effect of metallurgical evolution during post-weld aging treatment on localised corrosion of resistance spot welding joints of A286 superalloy. *Corros. Eng. Sci. Technol.* **2018**, *53*, 355–361. [CrossRef]
28. Tam, S.C.; Williams, R.; Yang, L.J.; Jana, S.; Lim, L.E.N.; Lau, M.W.S. A review of the laser processing of aircraft components. *J. Mater. Process. Technol.* **1990**, *23*, 177–194. [CrossRef]

29. Li, S.; Wei, Q.; Shi, Y.; Zhu, Z.; Zhang, D. Microstructure characteristics of Inconel 625 superalloy manufactured by selective laser melting. *J. Mater. Sci. Technol.* **2015**, *31*, 946–952. [CrossRef]
30. Jiang, C.; Liu, Z.-K. Computational investigation of constitutional liquation in Al–Cu alloys. *Acta Mater.* **2003**, *51*, 4447–4459. [CrossRef]
31. DuPont, J.N.; Lippold, J.C.; Kiser, S.D. *Welding Metallurgy and Weldability of Nickel Alloys*; John Wiley & Sons: Hoboken, NJ, USA, 2005.